K. Iwamoto et al. / Int. J. Heat and Fluid Flow 23 (2002) 678 –689

Reynolds Number Effect on Wall Turbulence: Toward Effective Feedback Control

Kaoru IWAMOTO, Yuji SUZUKI, Nobuhide KASAGI

Department of Mechanical Engineering, The University of Tokyo

Hongo, Bunkyo-ku, Tokyo, 113-8656 Japan

iwamoto@thtlab.t.u-tokyo.ac.jp

ABSTRACT

Direct numerical simulation of turbulent channel flow at Re_τ= 110 ~ 650 is made in order to assess the feedback control algorithms which have been proposed for reducing skin friction. The effectiveness of the existing control schemes is decreased with increasing the Reynolds number from Re_τ= 110 to 300. It is found, through the Karhunen-Loeve (KL) decomposition of turbulent fluctuations, that the KL modes at $15 < y^+ < 30$, which correspond to longitudinal vortices and near-wall streaky structures, play a dominant role in the production of turbulence and wall shear stress at Re_τ = 110. At Re_τ = 300, however, the KL modes at $30 < y^+ < 75$ also make appreciable contribution to the wall shear stress generation. The regeneration mechanism of the near-wall vortices is related to the nonlinear interaction between the KL modes at $15 < y^+ < 30$ and those at $30 < y^+ < 75$.

Keywords: Wall Turbulence, Feedback Control, Skin Friction, Direct Numerical Simulation, Karhunen-Loeve Decomposition

1. INTRODUCTION

Up to now, various Reynolds number effects in wall turbulence have been reported. Zagarola

& Smits (1998) suggest that the overlap region between inner and outer scalings in wall-bounded turbulence may yield a power law rather than a log law at very high Reynolds numbers. Moser *et al*. (1999) have made direct numerical simulation (DNS) of fully-developed turbulent channel flow at $Re_\tau = 180 \sim 590$, which is defined based on the wall friction velocity u_τ, the channel half-width δ and kinematic viscosity ν. They conclude that the wall-limiting behavior of root-mean-square (rms) velocity fluctuations strongly depends on the Reynolds number, but obvious low-Reynolds-number effects are absent at $Re_\tau > 395$. It is well known that near-wall streamwise vortices play an important role in the transport mechanisms in wall turbulence, at least, at low Reynolds number flows (see, e.g., Robinson, 1991; Kasagi *et al*., 1995; Kravchenko *et al*., 1993). Those streamwise vortices and streaky structures, which are scaled with viscous wall units (e.g., Kline *et al*., 1967), are closely associated and regenerated through inherent near-wall mechanisms (e.g., Hamilton *et al*., 1995). On the other hand, characteristics of near-wall coherent structures at higher Reynolds numbers still remain unresolved. Adrian *et al*. (2000) show that packets of large-scale hairpin vortices are often observed in high-Reynolds-number wall turbulence.

From a viewpoint of saving energy and protecting the environment, it is needed to develop efficient turbulence control techniques for drag reduction and/or heat transfer augmentation. Among various methodologies, active feedback control scheme attracts much attention because of its large control effect with small power input (Moin & Bewley, 1994; Gad-el-Hak, 1996; Kasagi, 1998). Choi *et al*. (1994) employed local blowing/suction on the wall, which is exerted to oppose the wall-normal velocity fluctuation in the buffer layer (V-control), and obtained approximately 25% drag reduction in their DNS of turbulent channel flow. Bewley *et al*. (1993) applied a suboptimal control scheme (Choi *et al.,* 1993) to turbulent channel flow, and obtained about 17% drag reduction. Furthermore, Bewley *et al*. (2001) showed that the turbulent channel flow could be ultimately relaminarized by an optimal control scheme. Although these control schemes have demonstrated marked effectiveness, they are difficult to employ. It is because they inevitably require sensing at numerous points inside the flow field, which is not feasible in real applications.

Recently, control algorithms using only flow variables at the wall have been developed. Lee

et al. (1998) proposed a suboptimal control algorithm based on the linearized Navier-Stokes equation, and obtained a simple analytical formula determining the control input based on the wall variables. Lee *et al*. (2001) proposed a reduced-order linear feedback controller based on the linearized two-dimensional Navier-Stokes equation, and obtained approximately 10% drag reduction in the DNS of turbulent channel flow. Furthermore, Endo *et al*. (2000) developed a control algorithm assuming arrayed wall shear stress sensors and wall deformable actuators of finite spatial dimensions, and achieved 10% drag reduction also in the DNS of channel flow.

The above pioneering studies have demonstrated that the active feedback control of wall turbulence is very much promising and can be implemented in a real system. However, the Reynolds numbers assumed in most previous studies are about $Re_\tau \sim 100$, where significant low-Reynolds-number effects must exist. Therefore, assessment of the existing control schemes at higher Reynolds numbers should be undertaken.

The final goal of the present work is to develop a control algorithm applicable to high Reynolds number flows. In the present study, two control algorithms for reducing skin friction are evaluated through DNS of turbulent channel flow at low-to-moderate Reynolds numbers. The contribution of coherent structures to the wall shear stress and nonlinear interactions between them are also examined through flow visualization and Karhunen-Loeve decomposition.

2. NUMERICAL METHOD AND CONTROL ALGORITHM

The numerical method used in the present study is almost the same as that of Kim *et al*. (1987); a pseudo-spectral method with Fourier series is employed in the streamwise (x) and spanwise (z) directions, while a Chebyshev polynomial expansion is used in the wall-normal (y) direction. A fourth-order Runge-Kutta scheme and a second-order Crank-Nicolson scheme are used for time discretization of the nonlinear terms and the viscous terms, respectively. The computational conditions are summarized in Table 1. The Reynolds number Re_τ is chosen as 110, 150, 300, 400, and 650. The flow rate is kept constant at each Reynolds number. Although it is not shown here, turbulence statistics of the present computation for plane channel flow are in good agreement with the DNS data of Moser *et al*. (1999), and are available on the web page at http://www.thtlab.t.u-tokyo.ac.jp. Hereafter, u, v, and w denote the velocity components in

the x-, y-, and z-directions, respectively. Superscript (+) represents quantities non-dimensionalized with u_τ and ν.

In order to evaluate the efficiency of feedback control algorithms at various Reynolds numbers, V-control scheme (Choi *et al.,* 1994) and the suboptimal control (Lee *et al.,* 1998) are adopted. In both cases, the control input is local blowing/suction at the wall. In the V-control, it is given as:

$$v^+_{wall} = -\alpha v^+\Big|_{y^+=10}. \tag{1}$$

For the suboptimal control scheme, square of the wall-normal gradient of the spanwise velocity is included in the cost function, and this leads to the control input:

$$\hat{v}^+_{wall} = \alpha \frac{ik_z}{k} \frac{\partial \hat{w}^+}{\partial y^+}\bigg|_{wall}, \quad k = \left(k_x^2 + k_z^2\right)^{1/2}, \tag{2}$$

where (^) denotes the Fourier coefficient. In Eq. (2), k_x and k_z denote wavenumbers in the x- and z-directions, respectively. The positive constant α is chosen in such a way that the power input is 0.05 ~ 0.4% of the pumping power. The power input P_{in} and the pumping power W are respectively defined as:

$$P_{in} \equiv \overline{p_{wall} v_{wall}} + 1/2 \cdot \rho \overline{v_{wall}{}^3}, \tag{3}$$

and

$$W \equiv -d\overline{P}/dx \cdot U_{mean}. \tag{4}$$

A fully developed flow field is used as the initial condition.

3. REYNOLDS NUMBER EFFECT ON FEEDBACK CONTROL

Figure 1 shows the drag reduction rate and the energy gain for the two tested control schemes versus Re_τ. Since the flow rate is kept constant, the drag reduction rate DR is given by

$$DR \equiv \left(W_0 - W\right)/W_0, \tag{5}$$

where W_0 denotes the pumping power for the unmanipulated flow. The energy gain G is defined

by the ratio of the pumping power saved to the power input:

$$G \equiv \left(W_0 - W\right)/P_{in}\,. \tag{6}$$

The present result at $\mathrm{Re}_\tau = 110$ is in good agreement with the DNS data of Choi *et al*. (1994) and Lee *et al*. (1998); the drag reduction of about 20% is achieved with $\alpha = 1$. For the *V*-control scheme with α kept constant, *DR* is decreased with increasing Re_τ and eventually seems to reach some asymptotic values. On the other hand, for the suboptimal control scheme, *DR* shows temporary increase and then decreases with increasing Re_τ. It is about 12% at $\mathrm{Re}_\tau = 650$ with $\alpha = 1$. This is probably because the suboptimal control algorithm is based on the linearized Navier-Stokes equation, although nonlinear interaction near the wall becomes more active with increasing Re_τ as described later. The gain, *G*, for both control schemes is critically diminished with increasing Re_τ, it eventually becomes insensitive to the Reynolds number at $\mathrm{Re}_\tau > 300$. Recently, Collis *et al*. (2000) made large eddy simulation of turbulent channel flow to assess the Reynolds number effect of *V*-control scheme and reported decrease in the control effectiveness with increasing the Reynolds number.

Figure 2 shows *DR* and *G* versus the power input ratio P_{in} / W_0, which means the fraction of the blowing/suction work against the pumping power spent to drive fluid in the channel. Unlike in Fig. 1, *DR* of the *V*-control scheme is decreased drastically as Re_τ is increased when P_{in} / W_0 is kept constant. However, *DR* gradually becomes insensitive to the Reynolds number at $\mathrm{Re}_\tau > 300$. The present result is in accordance with the findings of Moser *et al*. (1999) that obvious low-Reynolds-number effects are absent at $\mathrm{Re}_\tau > 300$. Note that the *V*-control scheme gives slightly larger DR than the suboptimal control scheme with the same P_{in} / W_0. When $\mathrm{Re}_\tau = 110$ and 150, *G* has a large peak at a small power input, and becomes as large as 100 - 200. When Re_τ is increased, however, *G* is also decreased. This is because the power input P_{in} is increased with Re_τ when achieving the same *DR*. As in Fig. 2(a), the gain for $\mathrm{Re}_\tau > 300$ is almost unchanged.

In all cases examined in this study, the power input P_{in} is nearly equal to the first term of RHS in Eq. (3), since the second term is less than 1% of P_{in} and should be negligible. Then, P_{in} can be rewritten as:

$$P_{in}^{+} \approx \overline{p_{wall}{}^{+} v_{wall}{}^{+}} = p_{rms,wall}{}^{+} \cdot v_{rms,wall}{}^{+} \cdot R_{pv,wall}, \tag{7}$$

where $R_{pv,wall}$ is the correlation coefficient between p and v on the wall. Figure 3 shows the rms fluctuations of p and v on the wall, $p_{rms,wall}{}^{+}$ and $v_{rms,wall}{}^{+}$, against Re_τ. It is found that $p_{rms,wall}{}^{+}$ increases monotonically with Re_τ in both controlled and unmanipulated cases. The wall-normal velocity fluctuation $v_{rms,wall}{}^{+}$ is also increasing, but its growth rate is smaller than that of $p_{rms,wall}{}^{+}$ and it is even decreasing beyond $\mathrm{Re}_\tau = 400$ in the suboptimal control.

Figure 4 shows the correlation coefficient between the above mentioned quantities. For unmanipulated channel flows, $R_{pv,wall}$ estimated from the wall-limiting value is -0.35 ~ -0.4 at all Reynolds numbers examined, which is due to the effect of splatting (Lee & Hunt, 1991). On the other hand, $R_{pv,wall}$ for the controlled cases is positive and increased with Re_τ at $\mathrm{Re}_\tau < 300$, since wall blowing/suction determined by both control schemes is mostly opposed to the wall-normal velocity in the buffer layer. Therefore, the increase of P_{in} with Re_τ and hence the decrease of G at $\mathrm{Re}_\tau < 300$ shown in Fig. 2(b) are mainly owing to the increase of $p_{rms,wall}{}^{+}$ and $v_{rms,wall}{}^{+}$. Since $p_{rms,wall}{}^{+}$ is expected to increase continuously, control scheme for higher Reynolds numbers should keep $R_{pv,wall}$ negative or small positive in order to obtain large G.

From the present DNS results for both control schemes, low-Reynolds-number effects seem to be weak at $\mathrm{Re}_\tau > 300$. In the following chapter, we analyze the DNS database at $\mathrm{Re}_\tau = 110$ and 300 in order to study the underlying flow mechanisms, which result in the marked Reynolds number dependence presently explored. In particular, we focus on the so-called coherent structures near the wall such as quasi-streamwise vortices and longitudinal streaks (Kline *et al.*, 1967). We also try to obtain a clue for keeping control schemes effective at higher Reynolds number flows.

4. NONLINEAR INTERACTIONS BETWEEN COHERENT STRUCTURES

In order to investigate the contribution of coherent structures to the wall shear stress and transport mechanisms quantitatively, they are examined by using the Karhunen-Loeve decom-

position (Lumley, 1970).

4. 1 Karhunen-Loeve Decomposition

The Karhunen-Loeve theory is based on the decomposition of the fluctuating velocity field into a sum of eigenfunctions φ_i of the two-point correlation tensor κ_{ij} (Lumley, 1981; Moin & Moser, 1989; Sirovich *et al*., 1990) as:

$$\int_0^{2\delta} \kappa_{ij}(y,y',m,n)\varphi_j(y',m,n)dy' = \lambda(m,n)\varphi_i(y), \quad i,j = 1 - 3, \tag{8}$$

where m and n respectively denote wavenumbers in the x- and z-directions, while λ denotes the eigenvalue. The total number of eigenvalues for wavenumber index pairs (m, n) is three times of N_y, which is the number of grid points in the y-direction. Each eigenfunction is specified with a triplet $\mathbf{k} = (m, n, q)$ (Webber *et al*., 1997). The three-dimensional eigenfuction is a complex valued vector field, which can be written as:

$$\boldsymbol{\phi}^{\mathbf{k}}(x,y,z) = \boldsymbol{\varphi}^{\mathbf{k}}(y,m,n)e^{2\pi i(mx/L_x + nz/L_z)}. \tag{9}$$

Each eigenfunction satisfies the incompressibility, the no-slip boundary condition and the orthogonality as:

$$\nabla \cdot \boldsymbol{\phi}^{\mathbf{k}} = 0, \tag{10}$$

$$\boldsymbol{\phi}^{\mathbf{k}} = \mathbf{0}, \quad \text{at } y = 0, 2\delta \tag{11}$$

$$\int_D \boldsymbol{\phi}^{\mathbf{k}} \cdot \tilde{\boldsymbol{\phi}}^{\mathbf{l}} d\boldsymbol{x} = \delta_{\mathbf{kl}}, \tag{12}$$

where (~) denotes the complex conjugate. Instantaneous velocity field can be decomposed as a linear superposition of the eigenfucntions as follows:

$$\boldsymbol{u}(x,y,z,t) = \sum_{\mathbf{k}} a^{\mathbf{k}}(t)\boldsymbol{\phi}^{\mathbf{k}}(x,y,z). \tag{13}$$

Note that the eigenvalues $\lambda^{\mathbf{k}}$ represent the energy in each KL mode (Lumley, 1981), so that eigenfunctions can be sorted according to their contribution to the turbulent kinetic energy.

4. 2 Turbulent Kinetic Energy of KL Modes

Figure 5 shows the most energetic eigenfunctions among the KL modes for Re_τ = 110 and 300. For both Reynolds numbers, there are large-scale low- and high-speed regions, which are homogeneous in the streamwise direction, and associated with large streamwise vortices. This fact is in accordance with the result of Webber *et al*. (1997) for the minimal channel flow (Jimenez & Moin, 1991) at Re_τ = 136. To represent 50% of the total kinetic energy, 190 and 340 eigenvalues are required for Re_τ = 110 and 300, respectively. Although it is not shown here, most KL modes exhibit vortical structures. In the present study, wall elevation of these structure is characterized with the center of the vortices for each KL mode defined by the global minimum of the second invariant of the deformation tensor. For the most energetic modes shown in Fig. 5, the location of the center of the vortices y_v^+ is about 50 at Re_τ = 110 and about 120 at Re_τ = 300, respectively.

Figure 6 shows the fractional contribution of KL modes at each y_v to the total turbulent kinetic energy in the flow volume. Note that the integration of the fractional contribution over the channel width is equal to unity. It is found that y_v is scaled with δ at $y_v / \delta > 0.5$, but is not near the wall. Therefore, the degree of contribution of the decomposed structures to the turbulent kinetic energy can not be scaled with a single length scale.

4. 3 Contribution of KL Modes to Wall Shear Stress Fluctuation

In order to evaluate the contribution of KL modes to the wall shear stress fluctuation, the rms value of the wall shear stress $\tau_{w,rms}$ induced by each KL mode is computed. Figure 7 shows the eigenfunction with the largest contribution to $\tau_{w,rms}$ for Re_τ = 110 and 300. For both Reynolds numbers, low- and high-speed streaks and near-wall streamwise vortices are clearly observed. The center of the vortices, y_v^+, is 34 and 31 at Re_τ = 110 and 300, respectively. The spanwise spacing of these structures Δz^+ is about 138 and 134 at the two Re_τ, respectively, which is close to the average spacing of the streaky structures (~ 100). They are homogeneous (m = 0) in the streamwise direction at Re_τ = 110, but m = 1 at Re_τ = 300.

Figure 8 shows the fractional contribution of KL modes to $\tau_{w,rms}$. The contribution has a peak at about $y_v^+ = 23$ for both Reynolds numbers. Therefore, the structures having large contribution to the wall shear stress fluctuation are associated with the near-wall streamwise vortices scaled with the viscous wall unit. This result is in good qualitative agreement with Kravchenko *et al*. (1993), who have shown by using the two-point correlation of the wall shear stress and the streamwise vorticity that the wall shear stress is closely related to the near-wall streamwise vortices .

4. 4 KL Subgroups

In order to investigate the dynamics of turbulent coherent structures in detail, the KL modes are divided into subgroups depending on the location of the center of the vortices y_v. The n-th subgroup $\boldsymbol{u}^{<n>}$ is composed of linear superposition of the KL modes, of which y_v exist in between $(n - 1)\Delta y_v$ and $n\Delta y_v$:

$$\boldsymbol{u}^{<n>}(x,y,z,t) = \sum_{(n-1)\cdot\Delta y_v < y_v < n\cdot\Delta y_v} a^{\mathbf{k}}(t)\boldsymbol{\phi}^{\mathbf{k}}(x,y,z), \tag{14}$$

where $\Delta y_v^+ = 15$ for both $Re_\tau = 110$ and 300. Hence, the number of subgroups are 8 and 20 for $Re_\tau = 110$ and 300, respectively. Because of the linear superposition of the KL modes, each subgroup as a whole also satisfies the incompressibility, the no-slip boundary condition and the orthogonality.

Figure 9 shows a plane view (x - z) of an instantaneous flow field for $Re_\tau = 300$, in which both the near-wall vortical structures at $15 < y^+ < 30$ and those of the subgroup $\boldsymbol{u}^{<2>}$ are represented. Both of them are visualized with the 3-D contours of the second invariant of the deformation tensor Q^+ ($= u_{i,j}{}^+ u_{j,i}{}^+$) = -0.03. It is found that the trace of $\boldsymbol{u}^{<2>}$ almost always falls within the area of strong Q^+ of the original field. Thus, $\boldsymbol{u}^{<2>}$ mainly represents the instantaneous vortical structures at $15 < y^+ < 30$.

4. 5 Contribution of KL Subgroups to Reynolds Shear Stress

The Reynolds shear stress can be written using the KL subgroups as follows:

$$\overline{-u'v'} = \sum_n \overline{-u^{<n>}v^{<n>}} + \sum_m \sum_{n(\neq m)} \overline{-u^{<m>}v^{<n>}}, \tag{15}$$

where the first term of RHS corresponds to the correlation between the same KL subgroup, while the second term is that between different subgroups. Note that the latter is less than 1% of the former and is negligible.

Figure 10 shows the contribution of typical KL subgroups to the Reynolds shear stress. For $Re_\tau = 110$, $\boldsymbol{u}^{<2>}$ dominates close to the wall ($y^+ < 30$), while multiple $\boldsymbol{u}^{<n>}$ modes ($n \geq 3$) have comparable contributions at $y^+ > 30$. For $Re_\tau = 300$, the total Reynolds shear stress is increased mainly due to the increased contributions of $\boldsymbol{u}^{<3>}$ and $\boldsymbol{u}^{<4>}$, while that of $\boldsymbol{u}^{<2>}$ remains unchanged. The contribution of $\boldsymbol{u}^{<n>}$ ($n \geq 5$) is small at $y^+ < 30$ at both Reynolds numbers.

4. 6 Contribution of KL Subgroups to Mean Wall Shear Stress

The total shear stress τ in the turbulent channel flow is given as:

$$\tau = \mu \left.\frac{\partial \bar{u}}{\partial y}\right|_{wall} \left(1 - \frac{y}{\delta}\right) = \mu \frac{\partial \bar{u}}{\partial y} - \rho \overline{u'v'}. \tag{16}$$

The mean wall shear stress can be written with the bulk mean velocity and the Reynolds shear stress by integrating Eq. (16) twice in the y-direction (Fukagata & Kasagi, 2002) as:

$$\left.\frac{\partial \overline{u^+}}{\partial y^+}\right|_{wall} = \frac{3}{Re_\tau}\overline{u^+}_{mean} + \frac{3}{Re_\tau{}^2}\int_0^{\delta^+}\left(\int_0^{y^+} \overline{-u'^+v'^+}\, dy'^+\right) dy^+. \tag{17}$$

The first term of RHS represents the wall shear stress for the laminar flow with same flow rate. Because the flow rate is kept constant, the first term of RHS is also constant at each Reynolds number and is about 0.38 and 0.17 for $Re_\tau = 110$ and 300, respectively. The second term represents the contribution of the Reynolds shear stress to the wall shear stress. Thus, the second term of RHS must be decreased in order to reduce the wall shear stress.

Figure 11 shows the fractional contribution of each KL subgroup to the second term of RHS in Eq. (17). For $Re_\tau = 110$, the contribution of $\boldsymbol{u}^{<2>}$ is about 0.4, indicating that the drag reduction of about 40% could be achieved if $\boldsymbol{u}^{<2>}$ is completely suppressed. For $Re_\tau = 300$, on the other hand, the contribution of $\boldsymbol{u}^{<2>}$ is decreased to about 0.22, while those of $\boldsymbol{u}^{<3>}$ and

$\boldsymbol{u}^{<4>}$ are increased to about 0.15. Therefore, for $Re_\tau = 300$, $\boldsymbol{u}^{<2>}$ and $\boldsymbol{u}^{<3>}$ should also be suppressed in order to obtain the same degree of drag reduction. For both Reynolds numbers, the contributions of $\boldsymbol{u}^{<n>}$ ($n \geq 6$) are less than 0.04 and they are negligible.

4. 7 Nonlinear Interactions between KL Subgroups

The energy balance equation of $\boldsymbol{u}^{<n>}$ is derived as:

$$
\begin{aligned}
0 = & \sum_m \overline{-u_i^{+<n>} u_j^{+<m>}} \cdot \overline{u_{i,j}^{+}} - \sum_m \overline{u_{i,j}^{+<n>} u_{i,j}^{+<m>}} \\
& + \left(\overline{-u_j^{+<n>} p'^{+}} \right)_{,j} + \sum_m \left(\overline{u_i^{+<n>} u_{i,j}^{+<m>}} \right)_{,j} \\
& + \sum_m \left(\overline{-1/2 \cdot u_i^{+<n>} u_i^{+<n>} u_j^{+<m>}} \right)_{,j} + \sum_l \sum_{m(\neq n)} \left(\overline{-u_i^{+<n>} u_j^{+<l>} u_{i,j}^{+<m>}} \right),
\end{aligned}
\tag{18}
$$

where the six terms of RHS correspond to the production, dissipation, pressure diffusion, viscous diffusion, turbulent diffusion and nonlinear interaction between subgroups, sequentially. Strictly speaking, the over bar in Eq. (18) should be taken as the time-space average, because each subgroup satisfies the orthogonality only when integrated over the flow volume. However, averaging is presently made only over the x- and z-directions and time, since the residual of RHS is found negligible at each y-position without integration in the y-direction.

It is found that the production term (the first term of Eq. (18)) has a finite value only when $m = n$ (not shown), because each KL subgroup produces the Reynolds shear stress only with the same subgroup as mentioned above. In addition, the production has a large peak at $\boldsymbol{u}^{<2>}$, which is in accordance with the previous findings that turbulence producing event is located on the sides of near-wall vortices (Kasagi *et al.*, 1995). It is also noted that the dissipation term has non-zero value only when $m = n$.

Figure 12 shows the energy budget of $\boldsymbol{u}^{<2>}$ for $Re_\tau = 110$ and 300. For both Reynolds numbers, the distributions are similar to those of the total turbulent kinetic energy with the production term having a peak around $y^+ = 12$. On the other hand, the nonlinear interaction term, which represents the energy redistribution among KL subgroups, plays an important role in the energy balance of $\boldsymbol{u}^{<2>}$; it has negative values at $7 < y^+ < 45$ and its negative peak at $y^+ =$

20, where it is comparable to the dissipation term. Therefore, a part of the turbulent kinetic energy produced for $\boldsymbol{u}^{<2>}$ is transferred to other KL subgroups through the nonlinear interaction term, while the rest is dissipated in the near-wall region.

Figure 13 shows the nonlinear interaction term of each KL subgroup. When $Re_\tau = 110$, the subgroup of $\boldsymbol{u}^{<2>}$ loses its energy at $7 < y^+ < 45$, while $\boldsymbol{u}^{<1>}$ obtains the energy from other subgroups at $y^+ < 60$. The nonlinear interaction term for $\boldsymbol{u}^{<n>}$ ($n \geq 3$) is almost zero or only slightly positive near the wall. On the other hand, the positive peak of $\boldsymbol{u}^{<1>}$ is increased for $Re_\tau = 300$, whilst the profile of $\boldsymbol{u}^{<2>}$ is almost unchanged. Since $\boldsymbol{u}^{<n>}$ ($3 \leq n \leq 5$) becomes negative at $8 < y^+ < 50$, the energy should be transferred not only from $\boldsymbol{u}^{<2>}$, but also from $\boldsymbol{u}^{<n>}$ ($3 \leq n \leq 5$) to other KL subgroups (Fig. 13(b)).

Figure 14 shows the time-space integrals of the nonlinear interaction and the production term of each KL subgroup. For $Re_\tau = 110$, $\boldsymbol{u}^{<2>}$ has the largest production, and only the nonlinear interaction term of $\boldsymbol{u}^{<2>}$ is negative. Thus, the kinetic energy is transferred from $\boldsymbol{u}^{<2>}$ to other KL subgroups through the nonlinear interaction. Therefore, if $\boldsymbol{u}^{<2>}$, which represents the coherent structures with their centers at $15 < y^+ < 30$, is weakened by the control input, other subgroups should also be suppressed, since they do not have much direct energy production. For $Re_\tau = 300$, however, the production of $\boldsymbol{u}^{<n>}$ ($3 \leq n \leq 5$) is markedly increased, and their nonlinear interaction terms change the sign and become negative. Only $\boldsymbol{u}^{<1>}$ remains positive. Thus, a part of the turbulent kinetic energy generated at $30 < y^+ < 75$ should be transferred inward to the near-wall region.

Figure 15(a) shows contours of the time-space integrals of the nonlinear interaction term for $Re_\tau = 110$. The value at (l, m) for $\boldsymbol{u}^{<n>}$ corresponds to the energy transfer from $\boldsymbol{u}^{<m>}$ to $\boldsymbol{u}^{<n>}$ through the nonlinear interaction with $\boldsymbol{u}^{<l>}$. For $\boldsymbol{u}^{<1>}$, one positive peak is observed at (l, m) = (2, 2) and no negative value is observed, indicating that the nonlinear interaction term of $\boldsymbol{u}^{<1>}$ always acts as gain. For $\boldsymbol{u}^{<2>}$, two negative peaks are observed at (l, m) = (2, 1) and (2, 3), and no positive value is observed. Thus, the kinetic energy of $\boldsymbol{u}^{<2>}$ is mainly transferred to $\boldsymbol{u}^{<1>}$ and $\boldsymbol{u}^{<3>}$ through the nonlinear interaction with itself. On the other hand, $\boldsymbol{u}^{<3>}$ has one positive and one negative peaks at (l, m) = (2, 2) and (2, 1), respectively. The net nonlinear interaction term for $\boldsymbol{u}^{<3>}$ acts as gain from $\boldsymbol{u}^{<2>}$ as shown in Fig. 14, but a part of its energy is transferred

to $\boldsymbol{u}^{<1>}$ through the interaction with $\boldsymbol{u}^{<2>}$.

Figure 15(b) shows contours of the nonlinear interaction term for $Re_\tau = 300$. General trend is similar to that of $Re_\tau = 110$, but the positive region in $\boldsymbol{u}^{<1>}$ becomes more widely distributed at $l < 4$ and $m < 4$. The energy transfer of $\boldsymbol{u}^{<2>}$ to $\boldsymbol{u}^{<3>}$ is decreased, while that of $\boldsymbol{u}^{<3>}$ to $\boldsymbol{u}^{<1>}$ is increased. Therefore, the energy transfer from $\boldsymbol{u}^{<n>}$ to $\boldsymbol{u}^{<m>}$ ($n < m$), which corresponds to the outward energy transfer, becomes smaller, and the inward energy transfer from $\boldsymbol{u}^{<n>}$ to $\boldsymbol{u}^{<m>}$ ($n > m$) becomes larger.

It is noted that the mean and rms values of the nonlinear interaction of $\boldsymbol{u}^{<n>}$ ($n \leq 2$, i.e., $y_v^+ < 30$) is negligible at $l > 5$ or $m > 5$ ($y_v^+ > 75$) for both Reynolds numbers (not shown here). Therefore, the KL subgroups at $y_v^+ < 30$ are free from the nonlinear interaction from the KL subgroups at $y_v^+ > 75$.

Previous studies have shown that the near-wall structures are self-sustained through regeneration mechanisms (Brooke & Hanratty, 1993; Hamilton *et al*., 1995; Jeong *et al*., 1997). Recently, Jimenez & Pinelli (1999) claim that the damping of velocity fluctuations at $y^+ < 60$ results in laminarization, whilst the near-wall turbulence remains mostly unchanged when all the velocity fluctuations at $y^+ > 60$ are filtered out. The present findings with the KL decomposition clarify quantitatively that the near-wall turbulence mechanism depends only on the structures near th wall, say around $y^+ < 75$.

Figure 16 shows 3-D contours of the nonlinear interaction term of $\boldsymbol{u}^{<2>}$ in an instantaneous flow field at $Re_\tau = 300$. The energy transfer from $\boldsymbol{u}^{<2>}$ to other KL subgroups occurs on the sides of streamwise vortices, where the turbulence production is large. Positive regions, however, are located both upstream and downstream of the streamwise vortices (e.g., A in Fig. 16). Brooke and Hanratty (1993) and Bernard *et al*. (1993) separately showed that new streamwise vortices emerge from these regions. Therefore, the energy transferred to $\boldsymbol{u}^{<2>}$ from other KL subgroups should contribute to the regeneration of the streamwise vortices.

4. 8 Reynolds number effect on wall turbulence

It is now clear that KL subgroups at $15 < y_v^+ < 30$, which correspond to the streamwise vortices, play a dominant role in the near-wall dynamics at both $Re_\tau = 110$ and 300, whilst the

structures at $y_v^+ > 75$ remain inactive. However, when $Re_\tau = 300$, the KL subgroups at $30 < y_v^+ < 75$ also play an important role; they carry finite contribution to the Reynolds stress and the wall shear stress, and a part of their energy produced is transferred inward to the near-wall structures through the nonlinear interaction. Therefore, not only the near-wall streamwise vortices ($y_v^+ < 30$) but also the structures at $30 < y_v^+ < 75$ should be manipulated in efficient feedback control scheme applicable to high Reynolds number flows.

5. CONCLUSIONS

Direct numerical simulation of turbulent channel flow was made in order to assess the performance of feedback control algorithms. KL decomposition is applied to examine quantitatively the effect of interaction between near-wall structures and structures away from the wall. The following conclusions are derived:

1) The *V*-control scheme offers substantial drag reduction rate for all Reynolds numbers examined, but the energy saving relative to the power input is markedly deteriorated when the Reynolds number is increased. It is chiefly owing to the increase of pressure fluctuaion on the wall. The same quantities of the suboptimal control scheme are smaller than those of *V*-control scheme at the same Reynolds number and power input.
2) The KL modes of large contribution to the wall shear stress fluctuation are accompanied with the near-wall streamwise vortices and associated streaky structures at $15 < y^+ < 30$, which are scaled with the wall units. The contribution of these structures to the mean wall shear stress are large, but that of the structures at $30 < y^+ < 75$ becomes larger with increasing the Reynolds number.
3) When $Re_\tau = 110$, the KL subgroup $\boldsymbol{u}^{<2>}$, which corresponds to the near-wall streamwise vortices, plays a dominant role in the Reynolds shear stress as well as turbulence production. Most of the turbulence energy is generated in $\boldsymbol{u}^{<2>}$ and redistributed toward/away from the wall. For $Re_\tau = 300$, not only $\boldsymbol{u}^{<2>}$ but also the structures at $30 < y^+ < 75$ become active. Therefore, those structures should be manipulated in efficient feedback control scheme for higher Reynolds number flows. However, structures at $y^+ > 75$ have little contribution to near-wall dynamics for both $Re_\tau = 110$ and 300.

4) The nonlinear energy transfer between near-wall KL modes becomes large in the region where the regeneration of streamwise vortices often occurs.

ACKNOWLEDGMENTS

This work was supported through the Project for Organized Research Combination System, and the Grant-in-Aid for Science Research on Priority Areas (B) by the Ministry of Education, Culture, Sports, Science and Technology of Japan (MEXT).

REFERENCES

Adrian, R. J., Meinhart, C. D., and Tomkins, C. D., 2000. Vortex organization in the outer region of the turbulent boundary layer. *J. Fluid Mech.* **422**, 1-54.

Bewley, T. R., Choi, H., Temam, R., and Moin, P., 1993. Optimal feedback control of turbulent channel flow. *CTR Annual Research Briefs* 3-14.

Bewley, T. R., Moin, P., and Temam, R., 2001. DNS-based predictive control of turbulence: an optimal benchmark for feedback algorithms. *J. Fluid Mech.* **447**, 179-225.

Brooke, J. W., and Hanratty, T. J., 1993. Origin of turbulence-producing eddies in a channel flow. *Phys. Fluids* A **5**, 1011-1021.

Bernard, P. S., Thomas, J. H., and Handler, R. A., 1993. Vortex dynamics and the production of Reynolds stress. *J. Fluid Mech.* **253**, 385-419.

Choi, H., Temam, R., Moin. P., and Kim, J., 1993. Feedback control for unsteady flow and its application to the stochastic Burgers equation. *J. Fluid Mech.* **253**, 509-543.

Choi, H., Moin, P., and Kim, J., 1994. Active turbulence control for drag reduction in wall-bounded flows. *J. Fluid Mech.* **262**, 75-110.

Collis, S. S., Chang, Y., Kellogg, S., and Prabhu, R. D., 2000. Large eddy simulation and turbulence control. *AIAA paper* 2000-2564.

Endo, T., Kasagi, N., and Suzuki, Y., 2000. Feedback control of wall turbulence with wall deformation. *Int. J. Heat & Fluid flow* **21**, 568-575.

Fukagata, K., and Kasagi, N., 2002. Active control for drag reduction in turbulent pipe flow.

5th Conf. on Engineering Turbulence Measurement and Modeling (ETMM5), Mallorca, Spain, 16-18 September 2002, to be presented.

Gad-el-Hak, M., 1996. Modern developments in flow control. *Appl. Mech. Rev.* **49**, 7, 365-379.

Hamilton, J. M., Kim, J., and Waleffe F., 1995. Regeneration mechanisms of near-wall turbulence structures. *J. Fluid Mech.* **287**, 317-348.

Jimenez, J., and Moin, P., 1991. The minimal flow unit in near-wall turbulence. *J. Fluid Mech.* **225**, 213-240.

Jimenez, J., and Pinelli, A., 1999. The autonomous cycle of near-wall turbulence. *J. Fluid Mech.* **389**, 335-359.

Jeong, J., Hussain, F., Schoppa, W., and Kim, J., 1997. Coherent structures near the wall in a turbulent channel flow. *J. Fluid Mech.* **332**, 185-214.

Kasagi, N., Sumitani, Y., Suzuki, Y., and Iida, O., 1995. Kinematics of the quasi-coherent vortical structure in near-wall turbulence. *Int. J. Heat & Fluid Flow* **16**, 2-10.

Kasagi, N., 1998. Progress in direct numerical simulation of turbulent transport and its control. *Int. J. Heat & Fluid flow* **19**, 125-134.

Kim, J., Moin, P., and Moser, R., 1987. Turbulence statistics in fully developed channel flow at low Reynolds number. *J. Fluid Mech.* **177**, 133-166.

Kline, S. J., Reynolds, W. C., Schraub, F. A., and Runstadler, P. W., 1967. The structure of turbulent boundary layers. *J. Fluid Mech.* **30**, 741-773.

Kravchenko, A. G., Choi, H., and Moin, P., 1993. On the relation of near-wall streamwise vortices to wall skin friction in turbulent boundary layers. *Phys. Fluids* A **5**, 12, 3307-3309.

Lee, C., Kim, J., and Choi, H., 1998. Suboptimal control of turbulent channel flow for drag reduction. *J. Fluid. Mech.* **358**, 245-258.

Lee, J. L., and Hunt, J. C. R., 1991. The structure of sheared turbulence near a plane boundary. *Turbulent Shear Flows* **7**, 101-118.

Lee, K. H., Cortelezzi, L., Kim, J., and Speyer, J., 2001. Application of reduced-order controller to turbulent flows for drag reduction. *Phys. Fluids* **13**, 1321-1330.

Lumley, J. L., 1970. *Stochastic tools in turbulence*. Academic.

Lumley, J. L., 1981. Coherent structures in turbulence. In *Transition and Turbulence* (ed. R. E. Meyer), 215-241, Academic.

Moin, P., and Moser, R., 1989. Characteristics-eddy decomposition of turbulence in a channel. *J. Fluid Mech.* **200**, 471-509.

Moin, P., and Bewley, T., 1994. Feedback control of turbulence. *Appl. Mech. Rev.* **47**, S3-S13.

Moser, R. D., Kim, J., and Mansour, N. N., 1999. Direct numerical simulation of turbulent channel flow up to $Re_\tau = 590$. *Phys. Fluids* **11**, 4, 943-945.

Robinson, S. K., 1991. The kinematics of turbulent boundary layer structure. *NASA TM* 103859.

Sirovich, L., Ball, K. S., and Keefe, L. R., 1990. Plane waves and structures in turbulent channel flow. *Phys. Fluids* A **2**, 2217-2226.

Webber, G. A., Handler, R. A., and Sirovich, L., 1997. The Karhunen-Loeve decomposition of minimal channel flow. *Phys. Fluids* **9**, 1054-1066.

Zagarola, M. V., and Smits, A. J., 1998. Mean-flow scaling of turbulent pipe flow. *J. Fluid Mech.* **373**, 33-79.

Figure captions

Figure 1 Dependence of drag reduction rate (a) and energy gain (b) on Reynolds number.

Figure 2 Drag reduction rate (a) and energy gain (b) versus power input ratio.

Figure 3 Rms pressure and wall-normal velocity fluctuations on the wall.

Figure 4 Correlation coefficient between pressure and wall-normal velocity component on the wall.

Figure 5 Most energetic eigenfunction among the KL modes. Isosurfaces of u'^+ and the second invariant of the deformation tensor Q^+ are shown. White, $u'^+ = 0.15$; Gray, $u'^+ = -015$; Black, $Q^+ = 0$. (a)$Re_\tau = 110$, (b)$Re_\tau = 300$.

Figure 6 Fractional contribution of KL modes at y_v to the total turbulent kinetic energy in the channel.

Figure 7 Eigenfunction of the largest contribution to $\tau_{w,rms}$; velocity vectors and contours of the streamwise velocity fluctuation u'^+ (Gray, $u'^+ > 0.15$; Black, $u'^+ < -015$). (a)$Re_\tau = 110$, (b)$Re_\tau = 300$.

Figure 8 Fractional contribution of KL modes at y_v^+ to $\tau_{w,rms}$.

Figure 9 Plane view of near-wall coherent structures for $Re_\tau = 300$ (Gray, the second invariant of the deformation tensor ($Q^+ < -0.03$) at $15 < y^+ < 30$; Black, the second invariant of the deformation tensor of $\boldsymbol{u}^{<2>}$ ($Q^+ < -0.03$)).

Figure 10 Contribution of KL subgroup to the Reynolds shear stress at $Re_\tau = 110$ and 300.

Figure 11 Fractional contribution of each KL subgroup to the wall friction increase beyond the laminar value.

Figure 12 Energy budget of $\boldsymbol{u}^{<2>}$ at $Re_\tau = 110$ and 300.

Figure 13 Nonlinear interaction term of each KL subgroup. (a)$Re_\tau = 110$, (b)$Re_\tau = 300$.

Figure 14 Time-space integrals of nonlinear interaction and production term of each KL subgroup at $Re_\tau = 110$ and 300.

Figure 15(a) Contours of time-space integrals of nonlinear interaction term for $Re_\tau = 110$. The contour levels range from -0.35 to 0.35 by increments of 0.02. Negative contours are dotted. (a-1) $\boldsymbol{u}^{<1>}$, (a-2) $\boldsymbol{u}^{<2>}$, (a-3) $\boldsymbol{u}^{<3>}$.

Figure 15(b) Contours of time-space integrals of nonlinear interaction term for $Re_\tau = 300$. The contour levels range from -0.4 to 0.4 by increments of 0.02. Negative contours are dotted. (b-1) $\boldsymbol{u}^{<1>}$, (b-2) $\boldsymbol{u}^{<2>}$, (b-3) $\boldsymbol{u}^{<3>}$.

Figure 16 Near-wall coherent structures and nonlinear interaction term of $\boldsymbol{u}^{<2>}$ at $Re_\tau = 300$ (White, the second invariant of the deformation tensor ($Q^+ < -0.03$); Black, positive nonlinear interaction term ($NL^+ > 0.5$); Black with mesh, negative nonlinear interaction term ($NL^+ < -0.5$)).

Table 1. Basic conditions of DNS of turbulent channel flow (Δy_c^+ is the y-interval at the channel center).

Re_τ	Computational periods		Grid points	Grid spacings		
	L_x	L_z	N_x, N_y, N_z	Δx^+	Δy_c^+	Δz^+
110	$5\pi\delta$	$2\pi\delta$	48, 65, 48	36.0	5.40	14.4
150	$2.5\pi\delta$	$\pi\delta$	64, 97, 64	18.4	4.91	7.36
300	$2.5\pi\delta$	$\pi\delta$	128, 193, 128	18.4	4.91	7.36
400	$2.5\pi\delta$	$\pi\delta$	192, 257, 192	16.4	4.91	6.54
650	$2.5\pi\delta$	$\pi\delta$	288, 257, 384	17.7	7.98	5.32

(a)

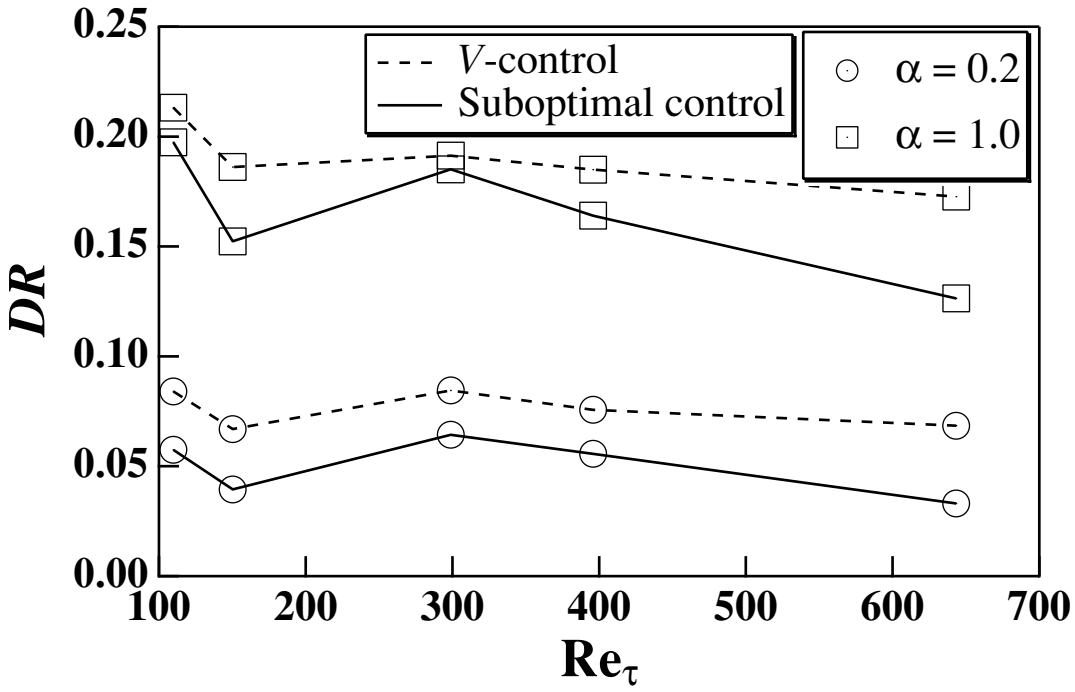

(b)

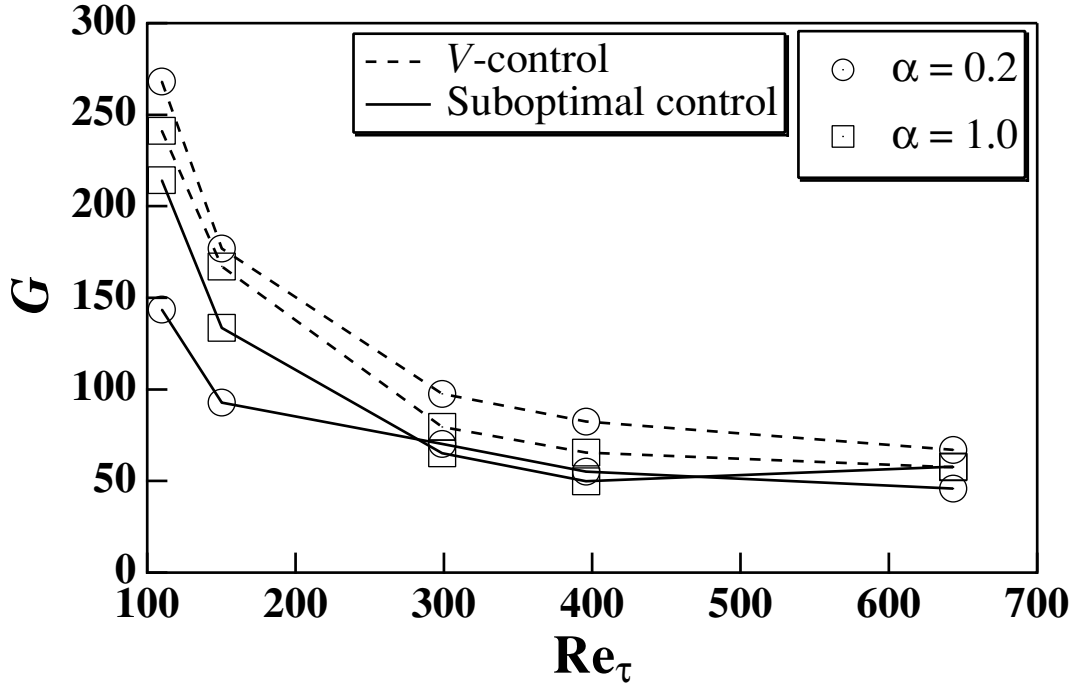

Figure 1 Dependence of drag reduction rate (a) and energy gain (b) on Reynolds number.

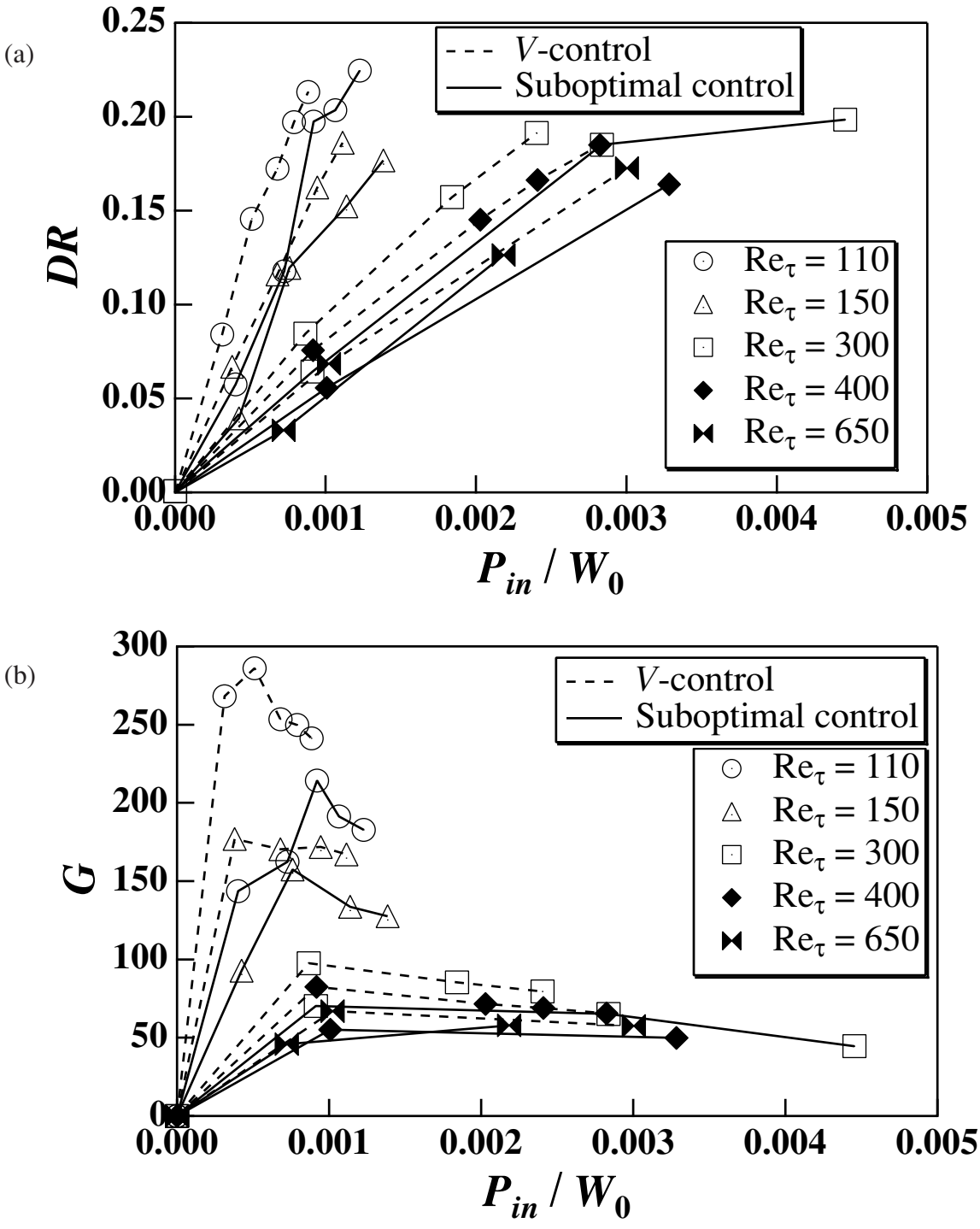

Figure 2 Drag reduction rate (a) and energy gain (b) versus power input ratio.

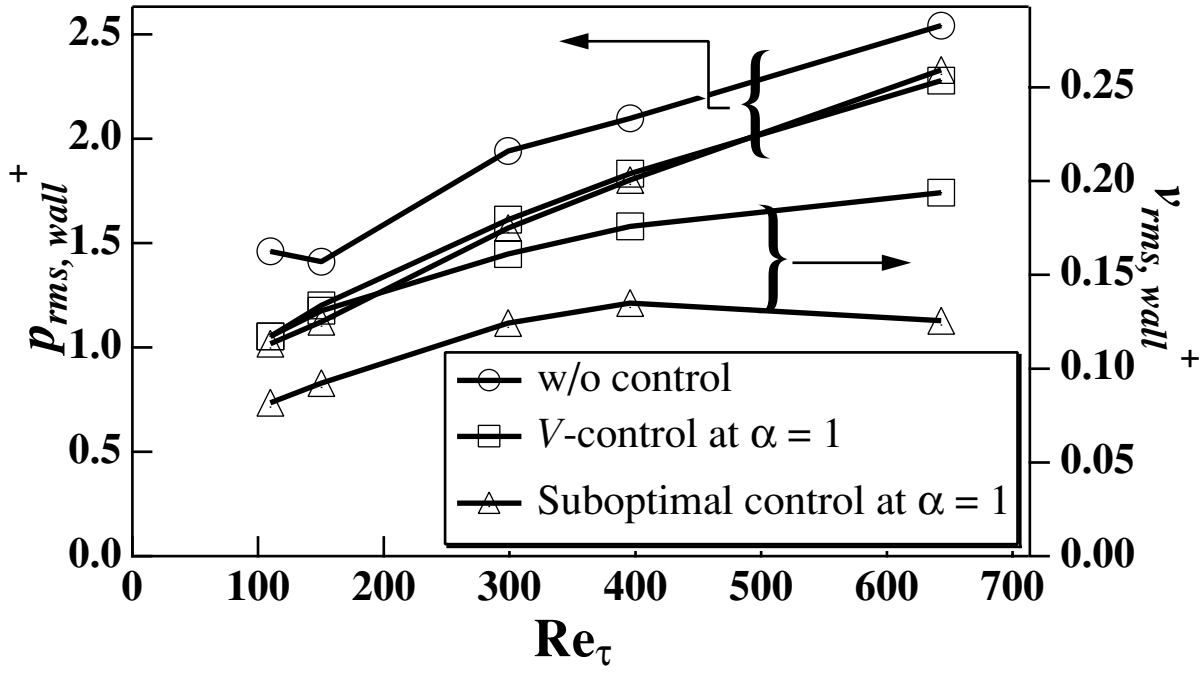

Figure 3 Rms pressure and wall-normal velocity fluctuations on the wall.

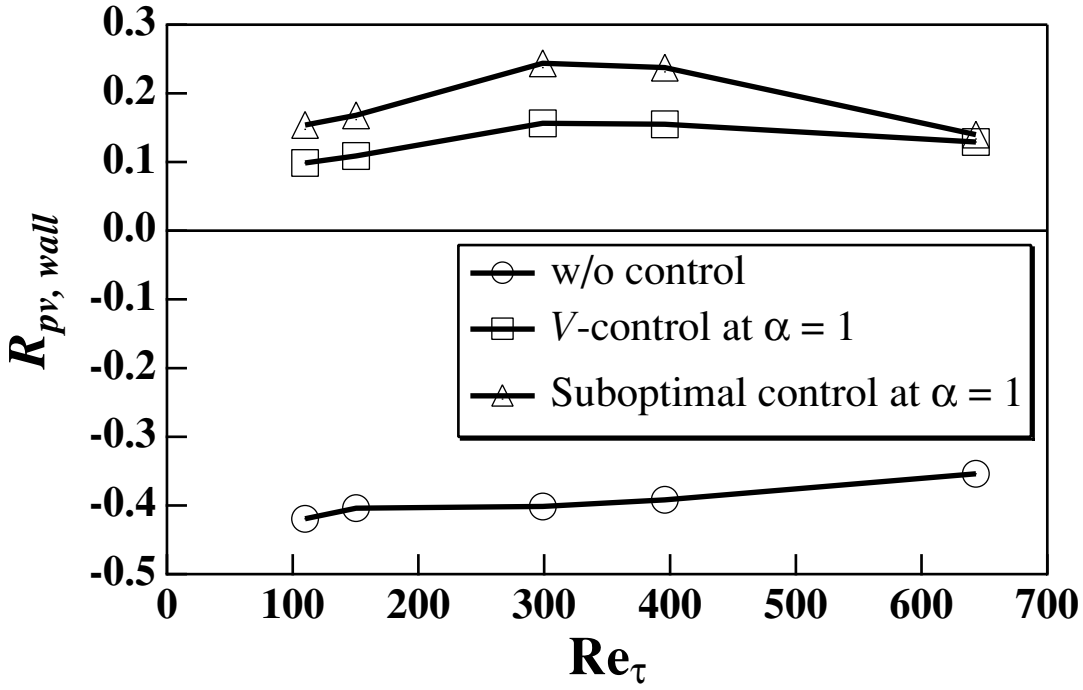

Figure 4 Correlation coefficient between pressure and wall-normal velocity component on the wall.

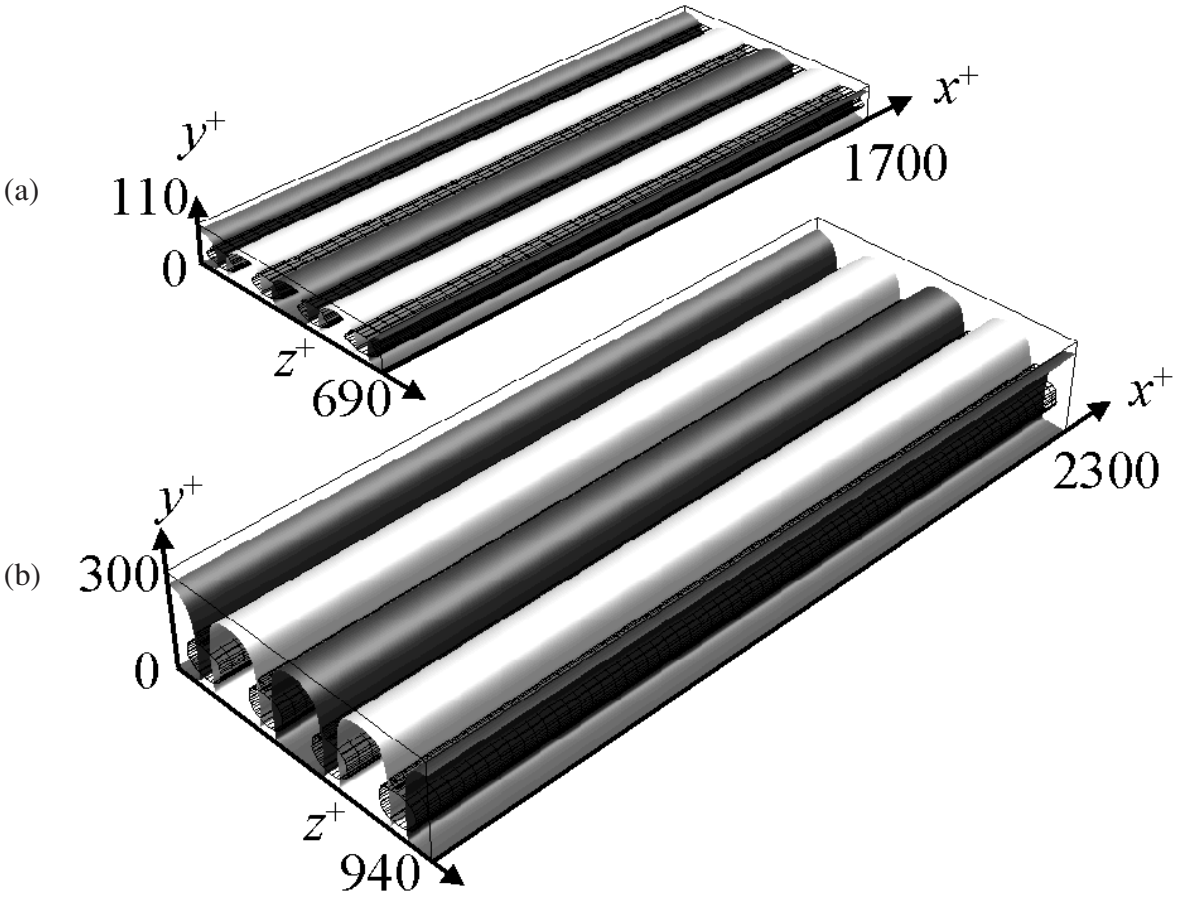

Figure 5 Most energetic eigenfunction among the KL modes. Isosurfaces of u'^+ and the second invariant of the deformation tensor Q^+ are shown. White, $u'^+ = 0.15$; black, $u'^+ = -015$; mesh, $Q^+ = 0$. (a)$Re_\tau = 110$, (b)$Re_\tau = 300$.

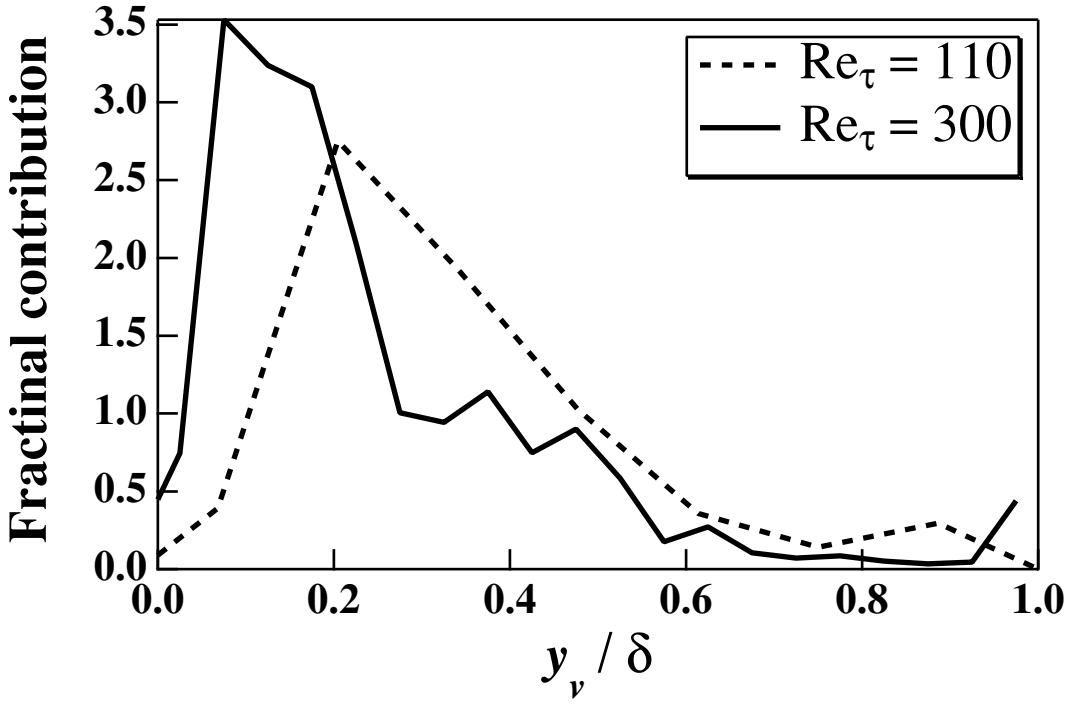

Figure 6 Fractional contribution of KL modes at y_v to the total turbulent kinetic energy in the channel.

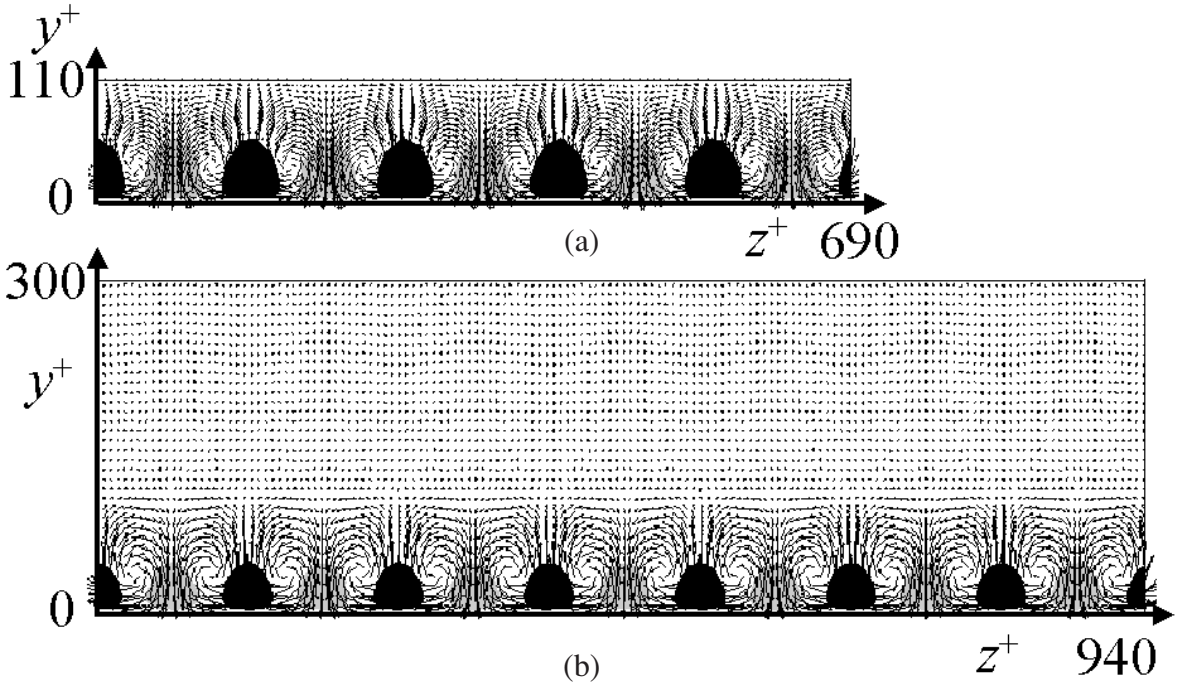

Figure 7 Eigenfunction of the largest contribution to $\tau_{w,rms}$; velocity vectors and contours of the streamwise velocity fluctuation u'^+ (gray, $u'^+ > 0.15$; black, $u'^+ < -015$). (a)$Re_\tau = 110$, (b)$Re_\tau = 300$.

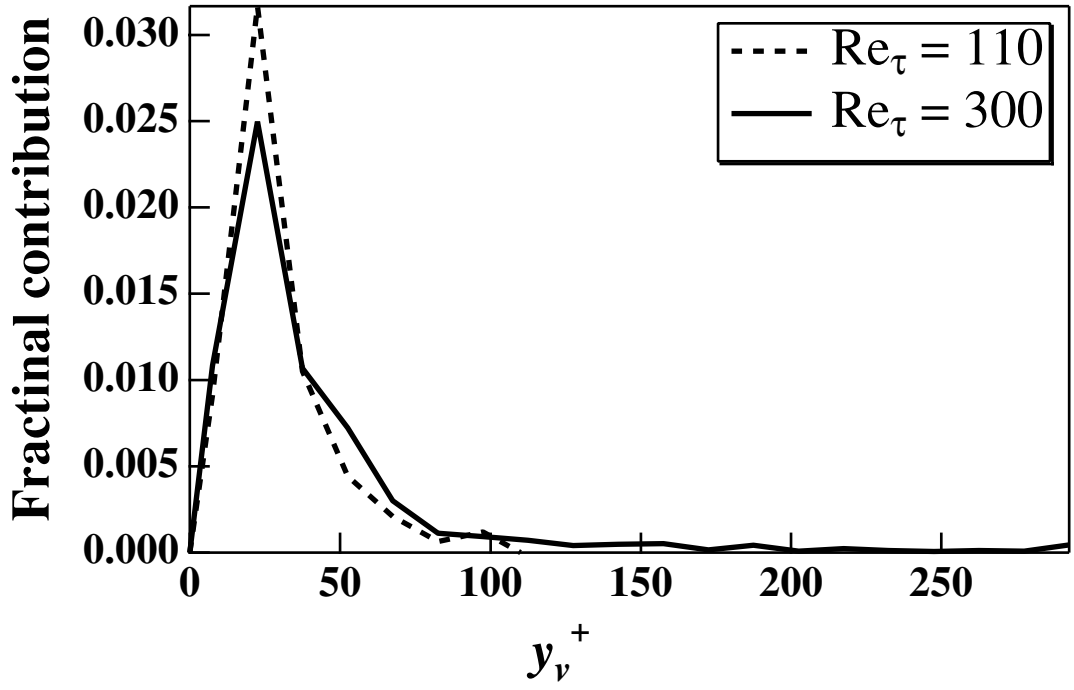

Figure 8 Fractional contribution of KL modes at y_v^+ to $\tau_{w,rms}$.

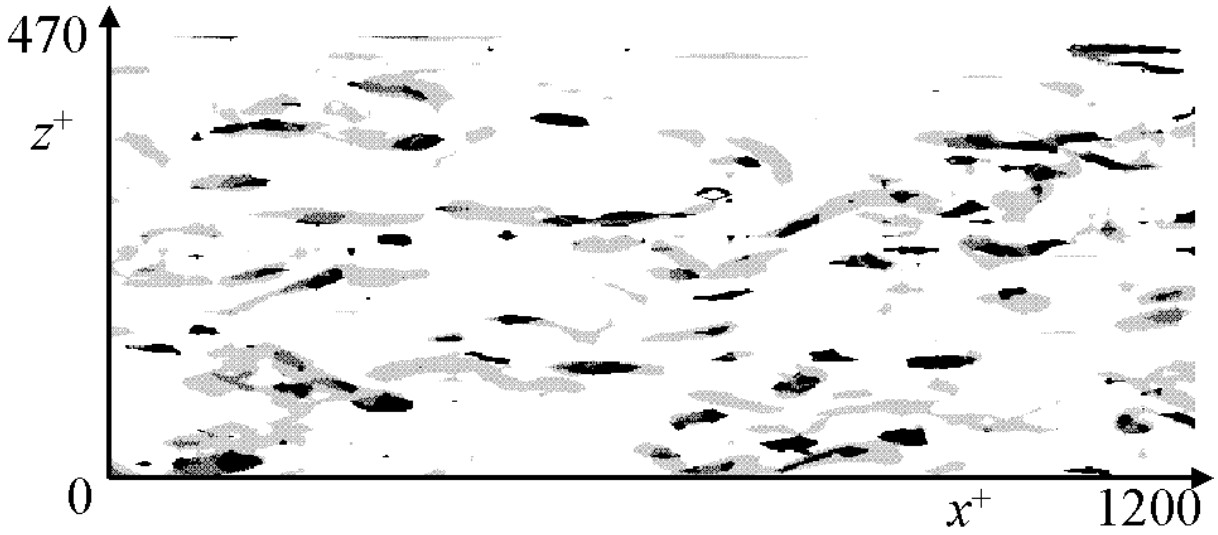

Figure 9 Plane view of near-wall coherent structures for $Re_\tau = 300$ (gray, the second invariant of the deformation tensor ($Q^+ < -0.03$) at $15 < y^+ < 30$; black, the second invariant of the deformation tensor of $\boldsymbol{u}^{<2>}$ ($Q^+ < -0.03$)).

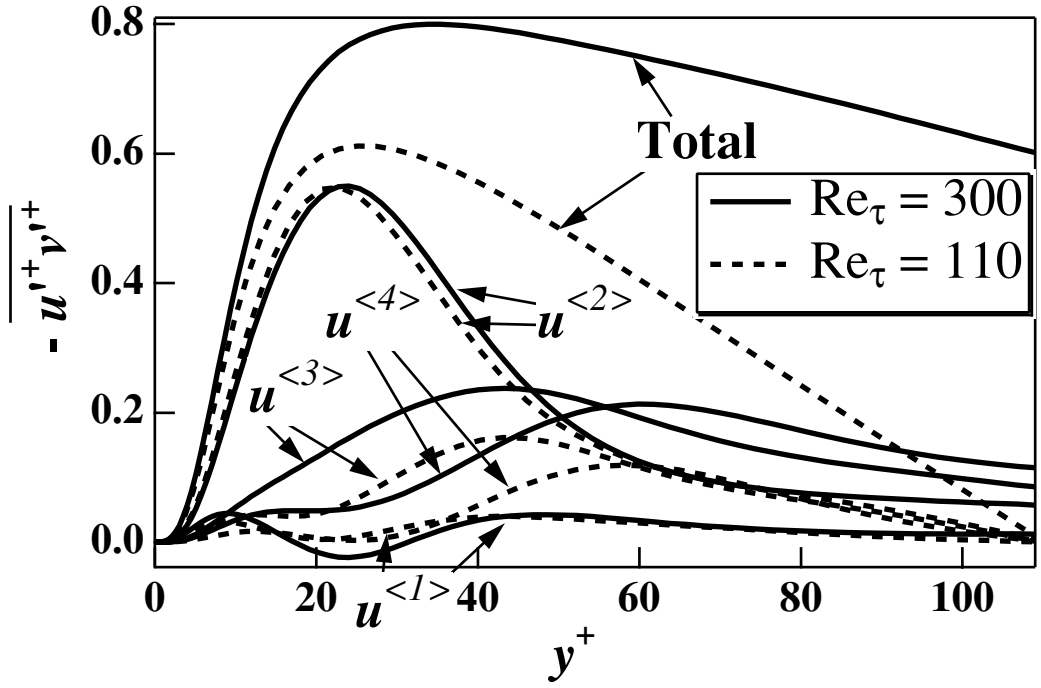

Figure 10 Contribution of KL subgroup to the Reynolds shear stress at $Re_\tau = 110$ and 300.

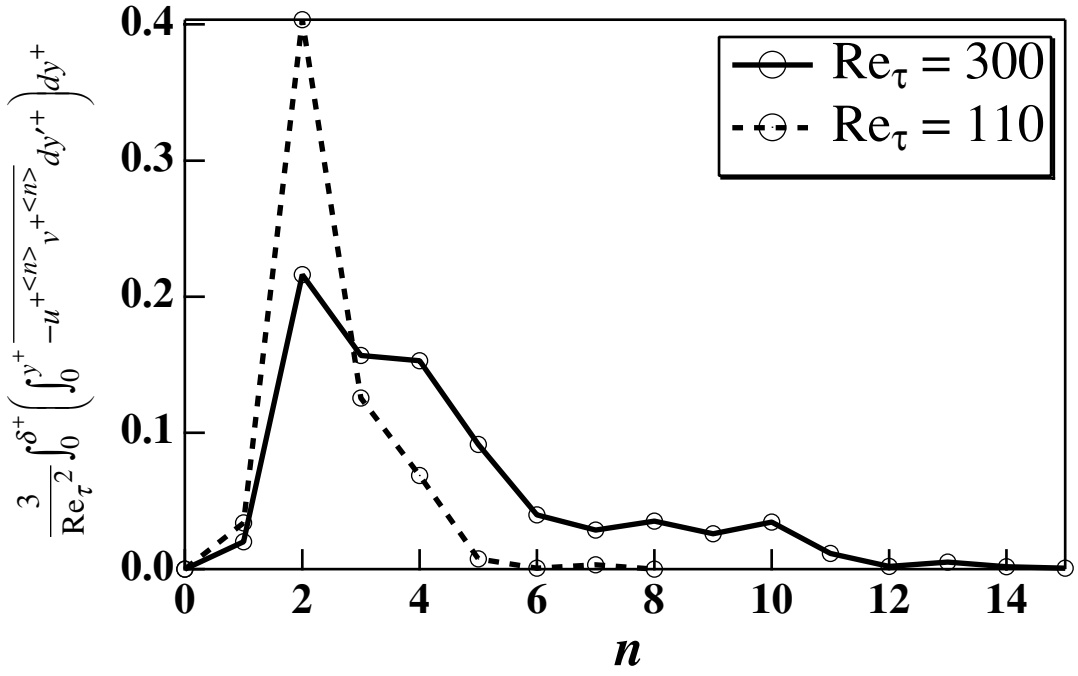

Figure 11 Fractional contribution of each KL subgroup to the wall friction increase beyond the laminar value.

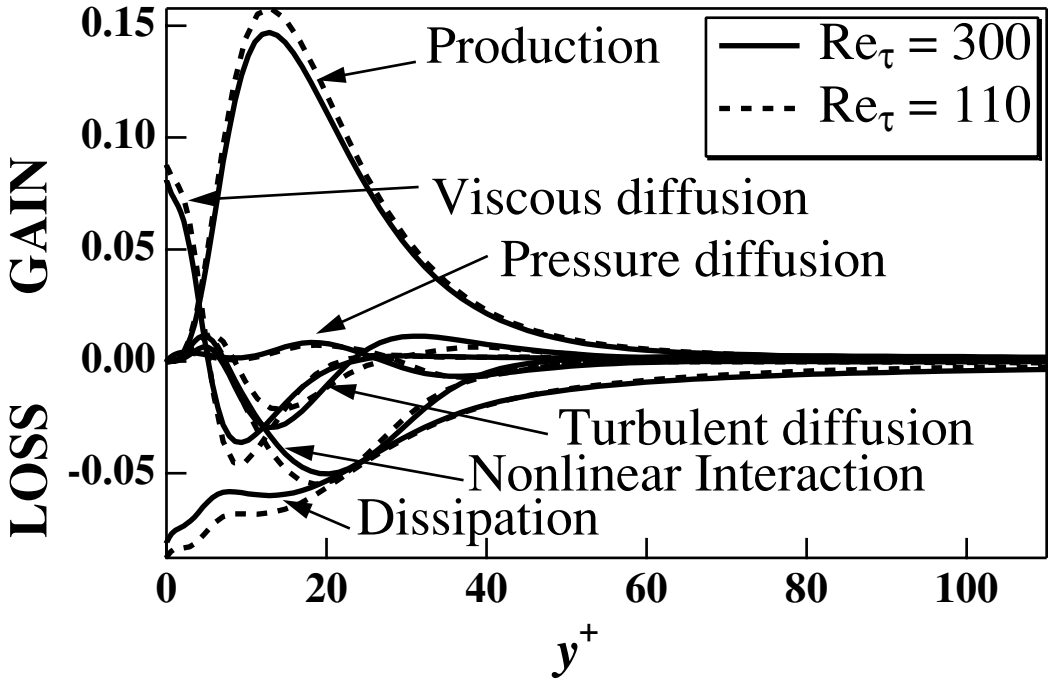

Figure 12 Energy budget of $\boldsymbol{u}^{<2>}$ at Re_τ = 110 and 300.

(a)

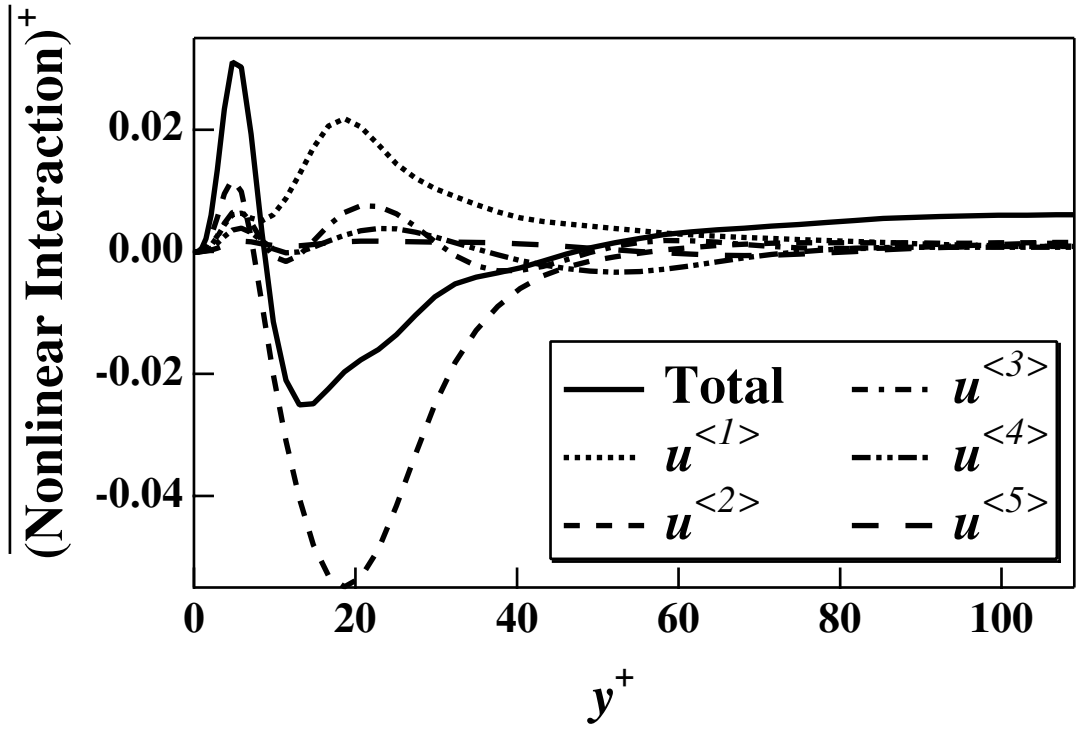

(b)

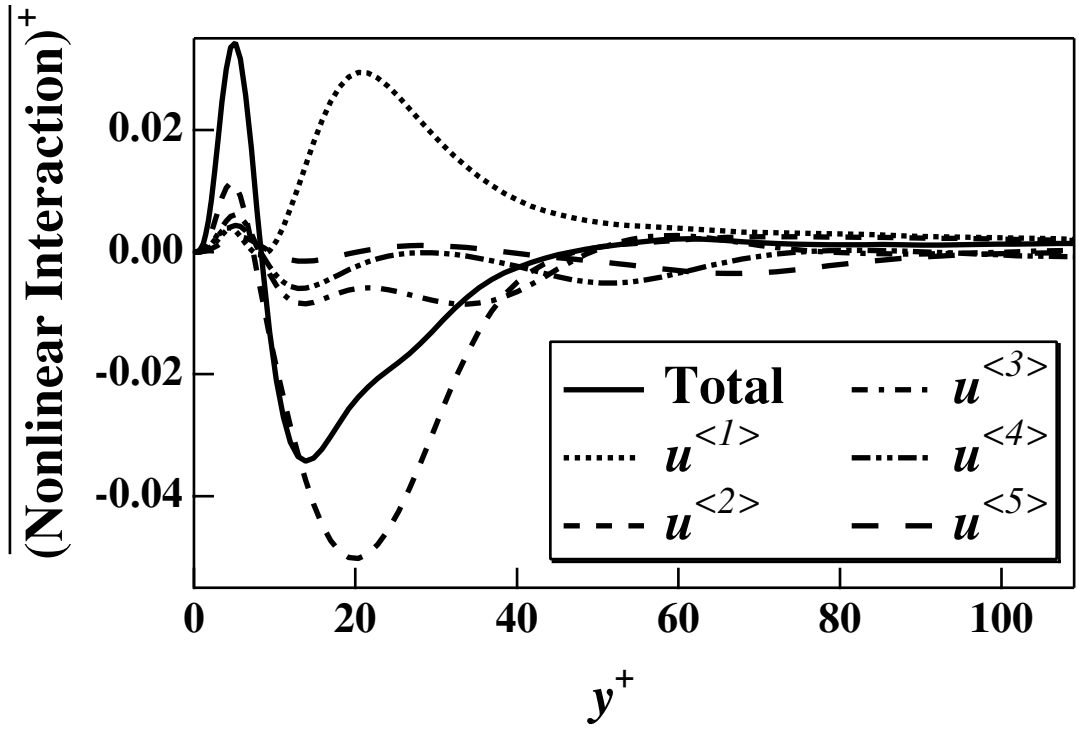

Figure 13 Nonlinear interaction term of each KL subgroup. (a)Re_τ = 110, (b)Re_τ = 300.

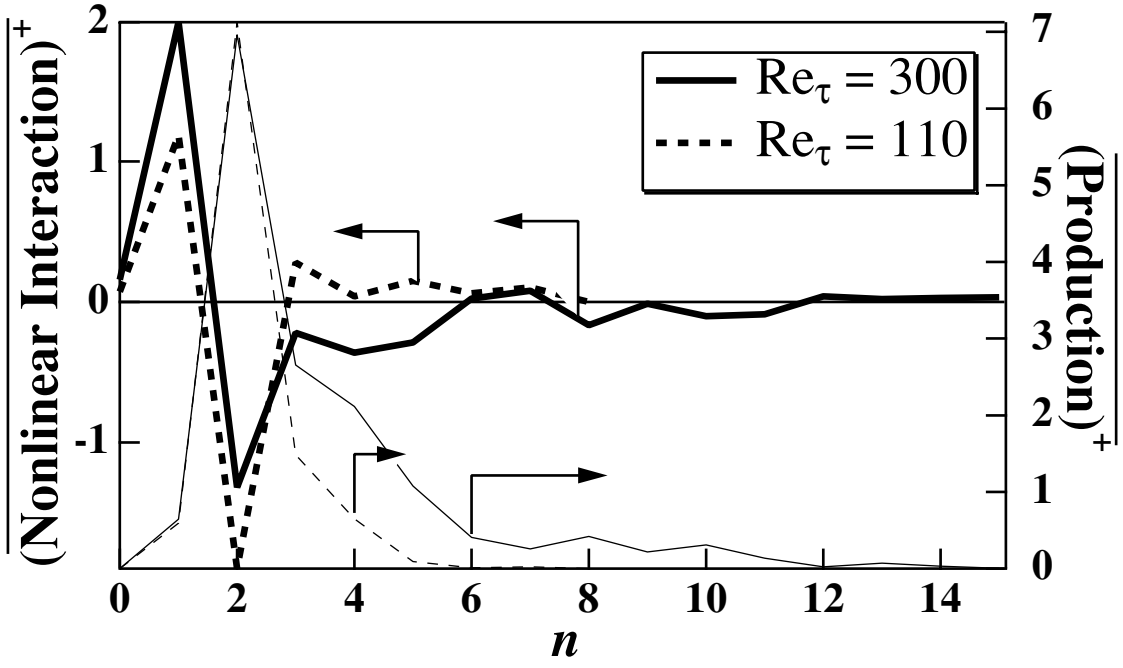

Figure 14 Time-space integrals of nonlinear interaction and production term of each KL sub-group at $Re_\tau = 110$ and 300.

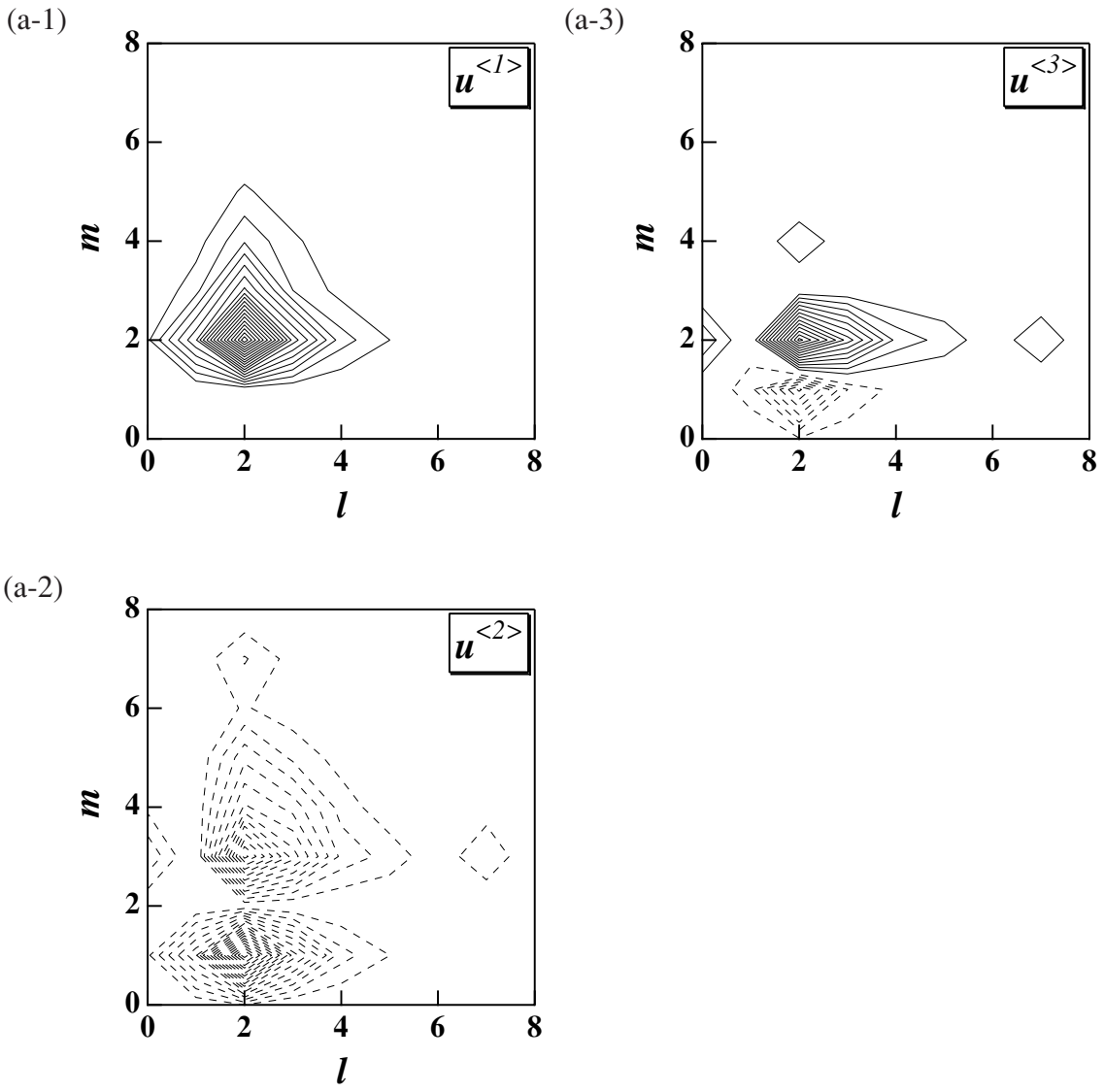

Figure 15(a) Contours of time-space integrals of nonlinear interaction term for $Re_\tau = 110$. The contour levels range from -0.35 to 0.35 by increments of 0.02. Negative contours are dotted. (a-1) $\boldsymbol{u}^{<1>}$, (a-2) $\boldsymbol{u}^{<2>}$, (a-3) $\boldsymbol{u}^{<3>}$.

(b-1)

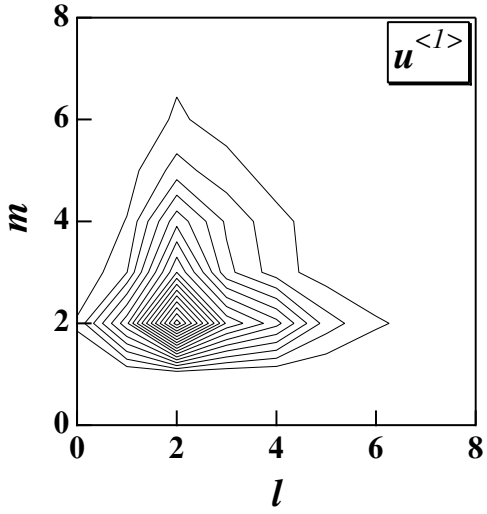

(b-3)

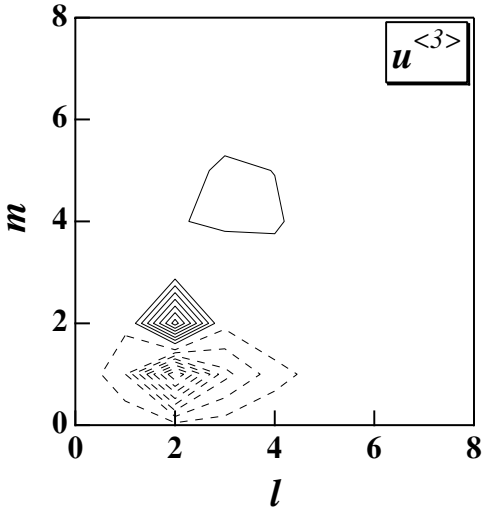

(b-2)

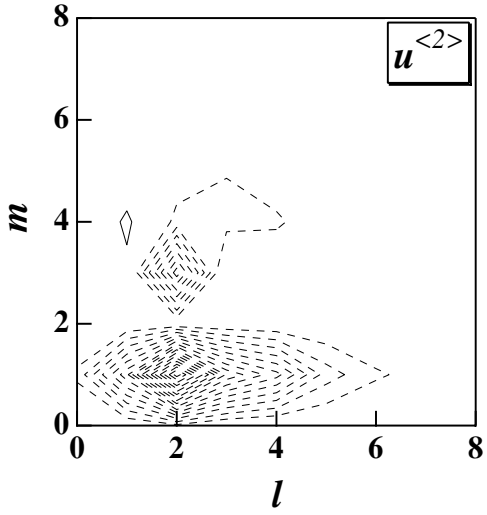

Figure 15(b) Contours of time-space integrals of nonlinear interaction term for $Re_\tau = 300$. The contour levels range from -0.4 to 0.4 by increments of 0.02. Negative contours are dotted. (b-1) $\boldsymbol{u}^{<1>}$, (b-2) $\boldsymbol{u}^{<2>}$, (b-3) $\boldsymbol{u}^{<3>}$.

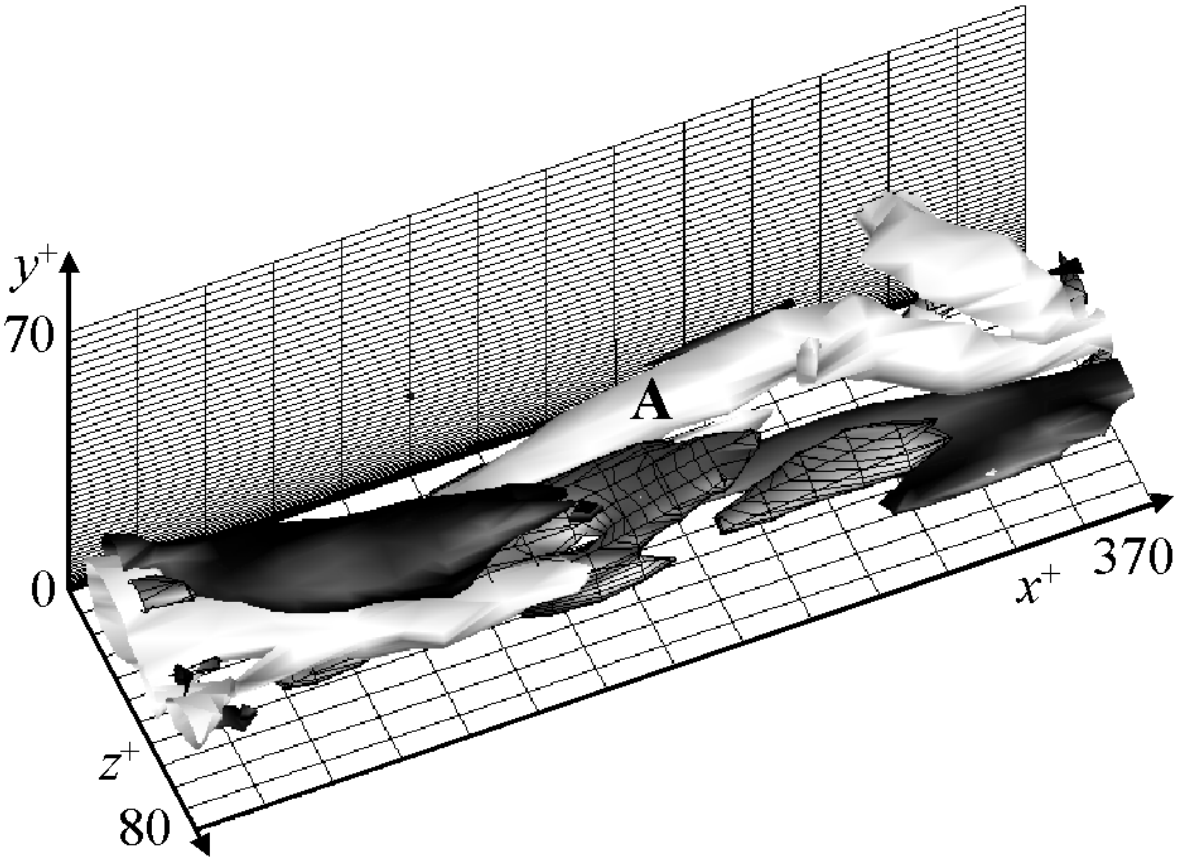

Figure 16 Near-wall coherent structures and nonlinear interaction term of $\boldsymbol{u}^{<2>}$ at $Re_\tau = 300$ (white, the second invariant of the deformation tensor ($Q^+ < -0.03$); black, positive nonlinear interaction term ($NL^+ > 0.5$); black with mesh, negative nonlinear interaction term ($NL^+ < -0.5$)).